A bending-gradient model for thick plates, II : Closed-form solutions for cylinfrical bending of laminates

Arthur Lebée, Karam Sab

A Bending-Gradient model for thick plates, Part II: Closed-form solutions for cylindrical bending of laminates

A. Lebée, K. Sab*

Université Paris-Est, Laboratoire Navier (ENPC/IFSTTAR/CNRS).
École des Ponts ParisTech, 6 et 8 avenue Blaise Pascal.
77455 Marne-la-Vallée, France
tel.+33-1-64153749, fax.+33-1-64153741,
e-mail: arthur.lebee@lami.enpc.fr, sab@enpc.fr

Abstract

In the first part (Lebée and Sab, 2010a) of this two-part paper we have presented a new plate theory for out-of-plane loaded thick plates where the static unknowns are those of the Kirchhoff-Love theory (3 in-plane stresses and 3 bending moments), to which six components are added representing the gradient of the bending moment. The new theory, called Bending-Gradient plate theory is an extension to arbitrarily layered plates of the Reissner-Mindlin plate theory which appears as a special case when the plate is homogeneous. Moreover, we demonstrated that, in the general case, the Bending-Gradient model cannot be reduced to a Reissner-Mindlin model. In this paper, the Bending-Gradient theory is applied to laminated plates and its predictions are compared to those of Reissner-Mindlin theory and to full 3D Pagano's exact solutions. The main conclusion is that the Bending-Gradient gives good predictions of deflection, shear stress distributions and in-plane displacement distributions in any material configuration. Moreover, under some symmetry conditions, the Bending-Gradient model coincides with the second-order approximation of the exact solution as the slenderness ratio L/h goes to infinity.

Key words: Plate Theory, Higher-order Models, Laminated Plates, Composite Plates

1. Introduction

Laminated plates are widely used in engineering applications. For instance angle-ply carbon fiber reinforced laminates are commonly used in aeronautics. However, these materials are strongly anisotropic and the plate overall behavior is difficult to capture. The most common plate theory is the Kirchhoff-Love plate model. However, it is well-known that, when the plate slenderness ratio L/h (h is the plate thickness and L the span) is not large enough, transverse shear stresses which are not taken into account in the Kirchhoff-Love theory have an increasing influence on the plate deflection.

In recent decades many suggestions have been made to improve the estimation of transverse shear stresses. Reddy (1989), Noor and Malik (2000) and Carrera (2002) provided detailed reviews for these models. Two main approaches can be found: asymptotic approaches and axiomatic approaches. The first one is mainly based on asymptotic expansions in the small parameter h/L (Caillerie, 1984; Lewinski, 1991c,b,a). However, higher-order terms yield only intricated "Kirchhoff-Love" plate equations and no distinction between relevant fields and unknowns was made. The second main approach is based on assuming *ad hoc* displacement or stress 3D fields. These models can be "Equivalent Single Layer" or "Layerwise". Equivalent single layer models treat the whole laminate as an equivalent homogeneous plate. However, when dealing with laminated plates, these models lead systematically to discontinuous transverse shear stress distributions through the thickness as indicated by Reddy (1989). In layerwise models, all plate degrees of freedom are introduced in each layer of the laminate and continuity conditions are enforced between layers. The reader can refer to Reddy (1989) and Carrera (2002) for detailed reviews of kinematic approaches and to (Naciri et al., 1998; Diaz Diaz et al., 2001; Hadj-Ahmed et al., 2001; Caron et al., 2006; Diaz Diaz et al., 2007; Dallot and Sab,

2008) for static approaches. Layerwise models lead to correct estimates of local 3D fields. However, their main drawback is that they involve a number of degrees of freedom proportional to the number of layers. The limitation is immediately pointed out with functionally graded materials, where the plate constituents properties vary continuously through the thickness (Nguyen et al., 2008a,b).

In the first part of this work (Lebée and Sab, 2010a) we revisited the use of 3D equilibrium in order to derive transverse shear stress as Reissner (1945) did for homogeneous plates. Thanks to standard variational tools, this led us to an Equivalent Single Layer plate theory which takes accurately into account shear effects and does not require any specific constitutive material symmetry: the Bending-Gradient theory. This plate theory is identical to the Reissner-Mindlin plate theory in the case of homogeneous plates. However, for laminated plates, shear forces are replaced by the gradient of the bending moment $\mathbf{R} = \boldsymbol{M} \otimes \boldsymbol{\nabla}$. Hence, this theory belongs to the family of higher-order gradient models. The mechanical meaning of the bending gradient was identified as self-equilibrated static unknowns associated to warping functions in addition to conventional shear forces.

The purpose of the present paper is to derive closed-form solutions for the Bending-Gradient model in the case of cylindrical bending and compare them to the exact solutions from Pagano (1969, 1970a,b) and to other approaches commonly used.

This paper is organized as follows. First, in Section 2, notations are briefly introduced. Then, in Section 3, the Bending-Gradient model is recalled, Voigt notation is introduced and the influence of material symmetries is also considered. In Section 4, cylindrical bending closed-form solutions are derived and applied to laminates. Finally, comparison with approximations based on Reissner-Mindlin theory and discussion on results are provided in Section 5.

2. Notations

Plate models involve 2-dimensional (2D) tensors of several orders. Vectors and higher-order tensors are boldfaced and different typefaces are used for each order: vectors are slanted: $\boldsymbol{T}$, $\boldsymbol{u}$. Second order tensors are sans-serif: $\boldsymbol{M}$, $\boldsymbol{e}$. Third order tensors are in typewriter style: $\boldsymbol{\Phi}$, $\boldsymbol{\Gamma}$. Fourth order tensors are in calligraphic style $\boldsymbol{\mathcal{D}}$, $\boldsymbol{\mathcal{C}}$. Sixth order tensors are double stroked $\mathbb{F}$, $\mathbb{W}$. For instance, the fourth-order tensor $\boldsymbol{\mathcal{C}} = \mathcal{C}_{\alpha\beta\gamma\delta}$ with Greek indexes $\alpha, \beta, \gamma.. = 1, 2$, denotes the plane-stress elasticity tensor. The identity for in-plane elasticity is $\mathcal{I}_{\alpha\beta\gamma\delta} = \frac{1}{2}\left(\delta_{\alpha\gamma}\delta_{\beta\delta} + \delta_{\alpha\delta}\delta_{\beta\gamma}\right)$, where $\delta_{\alpha\beta}$ is Kronecker symbol ($\delta_{\alpha\beta} = 1$ if $\alpha = \beta$, $\delta_{\alpha\beta} = 0$ otherwise). The transpose operation ${}^t\bullet$ is applied to any order tensors as follows: $\left({}^tA\right)_{\alpha\beta\ldots\psi\omega} = A_{\omega\psi\ldots\beta\alpha}$.

Three contraction products are defined, the usual dot product ($\boldsymbol{a} \cdot \boldsymbol{b} = a_\alpha b_\alpha$), the double contraction product ($\boldsymbol{a} : \boldsymbol{b} = a_{\alpha\beta} b_{\alpha\beta}$) and a triple contraction product ($\mathbf{A} \therefore \mathbf{B} = \mathtt{A}_{\alpha\beta\gamma}\mathtt{B}_{\gamma\beta\alpha}$). In these definitions Einstein's notation on repeated indexes is used. It should be noticed that closest indexes are summed together in contraction products. Thus, $\boldsymbol{\Phi} \cdot \boldsymbol{n} = \Phi_{\alpha\beta\gamma} n_\gamma$ is different from $\boldsymbol{n} \cdot \boldsymbol{\Phi} = n_\alpha \Phi_{\alpha\beta\gamma}$.

The derivation operator $\boldsymbol{\nabla}$ is also formally represented as a vector: $\boldsymbol{a} \cdot \boldsymbol{\nabla} = a_{\alpha\beta}\nabla_\beta = a_{\alpha\beta,\beta}$ is the divergence and $\boldsymbol{a} \otimes \boldsymbol{\nabla} = a_{\alpha\beta}\nabla_\gamma = a_{\alpha\beta,\gamma}$ is the gradient. Here $\otimes$ is the dyadic product.

In this paper, Voigt notation is also introduced. Brackets $[\bullet]$ are used to denote that a tensor is considered in a matrix form. Moreover, matrices and vectors of several dimensions are defined. Vectors and matrices are 2D by default. In other cases, $\tilde{\bullet}$ denotes dimension 3: $\tilde{\boldsymbol{U}}$ denotes a 3D vector and $\tilde{\boldsymbol{f}}$ denotes a 3×3 matrix. The related components are indexed with Latin indexes, $i, j, k.. = 1, 2, 3$: f_{ij}. $\hat{\bullet}$ denotes dimension 6: $\hat{\boldsymbol{P}}$ denotes a 6×6 matrix.

Finally, the integration through the thickness is noted $\langle\bullet\rangle$: $\int_{-\frac{h}{2}}^{\frac{h}{2}} f(x_3)dx_3 = \langle f \rangle$.

3. The Bending-Gradient plate model

3.1. Summary of the plate model

We consider a linear elastic plate of thickness h which mid-plane is the 2D domain $\omega \subset \mathbb{R}^2$ (Figure 1). Cartesian coordinates (x_1, x_2, x_3) in the reference frame $(\tilde{\boldsymbol{e}}_1, \tilde{\boldsymbol{e}}_2, \tilde{\boldsymbol{e}}_3)$ are used. The local stiffness tensor $\mathcal{C}_{ijkl}(x_3)$ is assumed to be invariant with respect to translations in the (x_1, x_2) plane and the plate is loaded exclusively with the out-of-plane distributed force $\tilde{\boldsymbol{p}} = p_3\tilde{\boldsymbol{e}}_3$.

The membrane stress $\boldsymbol{N}$, the bending moment $\boldsymbol{M}$, and shear forces $\boldsymbol{Q}$ are related to the actual 3D local stress by the following equations:

$$\begin{cases} N_{\alpha\beta}\left(x_1,x_2\right) = \langle \sigma_{\alpha\beta} \rangle & \text{(1a)} \\ M_{\alpha\beta}\left(x_1,x_2\right) = \langle x_3 \sigma_{\alpha\beta} \rangle & \text{(1b)} \\ Q_{\alpha}\left(x_1,x_2\right) = \langle \sigma_{\alpha 3} \rangle & \text{(1c)} \end{cases}$$

Moreover, we introduce the gradient of the bending moment $\mathbb{R} = \boldsymbol{M} \otimes \boldsymbol{\nabla}$. The 2D third-order tensor $\mathbb{R}$ complies with the following symmetry: $\mathtt{R}_{\alpha\beta\gamma} = \mathtt{R}_{\beta\alpha\gamma}$. It is possible to derive shear forces $\boldsymbol{Q}$ from $\mathbb{R}$ as: $\boldsymbol{Q} = \boldsymbol{i} \therefore \mathbb{R}$.

Equilibrium equations and boundary conditions involving stress fields were derived in Part I and are gathered in the set of statically compatible fields:

$$\begin{cases} \boldsymbol{N} \cdot \boldsymbol{\nabla} = \mathbf{o} \text{ on } \omega & \text{(2a)} \\ \boldsymbol{M} \otimes \boldsymbol{\nabla} - \mathbb{R} = 0 \text{ on } \omega & \text{(2b)} \\ (\boldsymbol{i} \therefore \mathbb{R}) \cdot \boldsymbol{\nabla} = -p_3 \text{ on } \omega & \text{(2c)} \\ \boldsymbol{N} \cdot \boldsymbol{n} = \boldsymbol{V}^d \text{ on } \partial\omega^s & \text{(2d)} \\ \boldsymbol{M} = \boldsymbol{M}^d \text{ on } \partial\omega^s & \text{(2e)} \\ (\boldsymbol{i} \therefore \mathbb{R}) \cdot \boldsymbol{n} = V_3^d \text{ on } \partial\omega^s & \text{(2f)} \end{cases}$$

where $\partial\omega^s$ is the portion of edge on which static boundary conditions apply: $\tilde{\boldsymbol{V}}^d$ is the force per unit length and $\boldsymbol{M}^d$ the full bending moment enforced on the edge. This set of equations is almost identical to Reissner-Mindlin equations where shear forces have been replaced by the bending gradient $\mathbb{R}$.

Generalized stresses $\boldsymbol{N}$, $\boldsymbol{M}$, and $\mathbb{R}$ work respectively with the associated strain variables: $\boldsymbol{e}$, the conventional membrane strain, $\boldsymbol{\chi}$ the curvature and $\boldsymbol{\Gamma}$ the generalized shear strain. These strain fields must comply with the following compatibility conditions and boundary conditions:

$$\begin{cases} \boldsymbol{e} = \boldsymbol{i} : (\boldsymbol{\nabla} \otimes \boldsymbol{U}) \text{ on } \omega & \text{(3a)} \\ \boldsymbol{\chi} = \boldsymbol{\Phi} \cdot \boldsymbol{\nabla} \text{ on } \omega & \text{(3b)} \\ \boldsymbol{\Gamma} = \boldsymbol{\Phi} + \boldsymbol{i} \cdot \boldsymbol{\nabla} U_3 \text{ on } \omega & \text{(3c)} \\ \boldsymbol{\Phi} \cdot \boldsymbol{n} = \boldsymbol{H}^d \text{ on } \partial\omega^k & \text{(3d)} \\ \tilde{\boldsymbol{U}} = \tilde{\boldsymbol{U}}^d \text{ on } \partial\omega^k & \text{(3e)} \end{cases}$$

where $\tilde{\boldsymbol{U}}$ is the average through the thickness of the 3D displacement of the plate and $\boldsymbol{\Phi}$ is the generalized rotation. $\boldsymbol{\Gamma}$ and $\boldsymbol{\Phi}$ are 2D third-order tensors with the following symmetry: $\Phi_{\alpha\beta\gamma} = \Phi_{\beta\alpha\gamma}$. Moreover, $\partial\omega^k$ is the portion of edge on which kinematic boundary conditions apply: $\tilde{\boldsymbol{U}}^d$ is a given displacement and $\boldsymbol{H}^d$ is a symmetric second-order tensor related to a forced rotation on the edge. These fields are almost identical to Reissner-Mindlin kinematically compatible fields where the rotation pseudo-vector is replaced by the generalized rotation $\boldsymbol{\Phi}$.

Finally, for constitutive material following local monoclinic symmetry with respect to (x_1, x_2) plane (uncoupling between $\mathbb{R}$ and $(\boldsymbol{N}, \boldsymbol{M})$) the Bending-Gradient plate constitutive equations are written as:

$$\begin{cases} \boldsymbol{N} = \boldsymbol{\mathcal{A}} : \boldsymbol{e} + \boldsymbol{\mathcal{B}} : \boldsymbol{\chi} & \text{(4a)} \\ \boldsymbol{M} = {}^t\boldsymbol{\mathcal{B}} : \boldsymbol{e} + \boldsymbol{\mathcal{D}} : \boldsymbol{\chi} & \text{(4b)} \\ \boldsymbol{\Gamma} = \mathbb{f} \therefore \mathbb{R}, \quad \text{where} \quad (\mathbb{I} - \mathbb{f} \therefore \mathbb{F}) \therefore \boldsymbol{\Gamma} = 0 & \text{(4c)} \end{cases}$$

where conventional Kirchhoff-Love stiffnesses are defined as $(\boldsymbol{\mathcal{A}}, \boldsymbol{\mathcal{B}}, \boldsymbol{\mathcal{D}}) = \left\langle \left(1, x_3, x_3^2\right) \boldsymbol{c}(x_3) \right\rangle$. The 2D sixth order tensors[1] $\mathbb{f}$ and $\mathbb{F}$ are the generalized shear compliance and stiffness. Their definition is detailed in

[1] $\mathtt{f}_{\alpha\beta\gamma\delta\epsilon\zeta}$ follows major symmetry: $\mathtt{f}_{\alpha\beta\gamma\delta\epsilon\zeta} = \mathtt{f}_{\zeta\epsilon\delta\gamma\beta\alpha}$ and minor symmetry $\mathtt{f}_{\alpha\beta\gamma\delta\epsilon\zeta} = \mathtt{f}_{\beta\alpha\gamma\delta\epsilon\zeta}$. Thus there are only 21 independent components

Section 4.2 of the present work. Moreover, $\mathbb{I}$ is the related identity tensor ($\mathbb{I}_{\alpha\beta\gamma\delta\epsilon\zeta} = i_{\alpha\beta\epsilon\zeta}\,\delta_{\gamma\delta}$). The solution of the plate model must comply with the three sets of equations (2, 3, 4). The compliance $\mathbb{f}$ is positive. However when $\mathbb{f}$ is not definite, there is a set of solutions, up to a self-stress field.

3.2. Voigt Notations

In this section, we introduce Voigt notation in order to turn contraction products into conventional matrix products. Brackets $[\bullet]$ are used to denote that a tensor is considered in a matrix form. Thus $[\bullet]$ is a linear operator, reallocating tensor components.

For instance, the bending moment is reallocated in a vector form:

$$[\boldsymbol{M}] = \begin{pmatrix} M_{11} \\ M_{22} \\ \sqrt{2}M_{12} \end{pmatrix} \tag{5}$$

as well as $\boldsymbol{N}$, $\boldsymbol{e}$ and $\boldsymbol{\chi}$, and the fourth-order compliance tensor $\mathbb{d}$ is reallocated in a matrix form so that constitutive equation (4b) becomes a vector-matrix product:

$$[\mathbb{d}] = \begin{pmatrix} d_{1111} & d_{2211} & \sqrt{2}d_{1211} \\ d_{2211} & d_{2222} & \sqrt{2}d_{1222} \\ \sqrt{2}d_{1211} & \sqrt{2}d_{1222} & 2d_{1212} \end{pmatrix} \tag{6}$$

as well as the stiffness tensor $\mathbb{D}$. This is also done to the other Kirchhoff-Love compliances $\mathbb{a}$, $\mathbb{b}$, and stiffnesses $\mathbb{A}$, $\mathbb{B}$ and also to the plane-stress stiffness tensor $\mathbb{c}$.

The same procedure is applied to shear variables and the corresponding constitutive equation. Shear static unknowns are reallocated in a vector form,

$$[\mathbb{R}] = \begin{pmatrix} \mathtt{R}_{111} \\ \mathtt{R}_{221} \\ \sqrt{2}\mathtt{R}_{121} \\ \mathtt{R}_{112} \\ \mathtt{R}_{222} \\ \sqrt{2}\mathtt{R}_{122} \end{pmatrix} \tag{7}$$

as well as $\mathbb{\Gamma}$ and $\mathbb{\Phi}$; and the constitutive sixth-order tensor is turned into a 6×6 matrix:

$$[\mathbb{f}] = \begin{pmatrix} \mathtt{f}_{111111} & \mathtt{f}_{111122} & \sqrt{2}\mathtt{f}_{111121} & \mathtt{f}_{111211} & \mathtt{f}_{111222} & \sqrt{2}\mathtt{f}_{111221} \\ \mathtt{f}_{221111} & \mathtt{f}_{221122} & \sqrt{2}\mathtt{f}_{221121} & \mathtt{f}_{221211} & \mathtt{f}_{221222} & \sqrt{2}\mathtt{f}_{221221} \\ \sqrt{2}\mathtt{f}_{121111} & \sqrt{2}\mathtt{f}_{121122} & 2\mathtt{f}_{121121} & \sqrt{2}\mathtt{f}_{121211} & \sqrt{2}\mathtt{f}_{121222} & 2\mathtt{f}_{121221} \\ \mathtt{f}_{112111} & \mathtt{f}_{112122} & \sqrt{2}\mathtt{f}_{112121} & \mathtt{f}_{112211} & \mathtt{f}_{112222} & \sqrt{2}\mathtt{f}_{112221} \\ \mathtt{f}_{222111} & \mathtt{f}_{222122} & \sqrt{2}\mathtt{f}_{222121} & \mathtt{f}_{222211} & \mathtt{f}_{222222} & \sqrt{2}\mathtt{f}_{222221} \\ \sqrt{2}\mathtt{f}_{122111} & \sqrt{2}\mathtt{f}_{122122} & 2\mathtt{f}_{122121} & \sqrt{2}\mathtt{f}_{122211} & \sqrt{2}\mathtt{f}_{122222} & 2\mathtt{f}_{122221} \end{pmatrix} \tag{8}$$

Finally, when using Voigt matrices components, the same typeface is used. The number of indexes indicates unambiguously whether it is the tensor component or the matrix component: $\mathtt{f}_{222221}$ is the tensor component of $\mathbb{f}$ and $\mathtt{f}_{56} = \sqrt{2}\mathtt{f}_{222221}$ is the matrix component of $[\mathbb{f}]$.

3.3. Symmetries

The effects of material symmetries on uncouplings have been presented in Part I. The main result is that $(\boldsymbol{N}, \boldsymbol{M})$ and bending gradient $(\mathbb{R})$ are uncoupled when the local elasticity tensor $\mathcal{C}_{ijkl}(x_3)$ follows monoclinic symmetry with respect to (x_1, x_2) plane for all x_3. Under this assumption, which is valid for most of applications involving laminated materials, it is possible to point out the influence of the invariance of the plate's overall configuration on the constitutive equations. Regarding the Kirchhoff-Love constitutive equation, we just recall that when the plate is overall symmetric with respect to its mid-plane there is

uncoupling between membrane stresses and bending moments: $\boldsymbol{\mathcal{B}} = \boldsymbol{0}$. This symmetry is often called mirror symmetry. Regarding the generalized shear constitutive equation, the in-plane transformations of $\mathbb{f}$ are identical to those for in-plane strain-gradient elasticity. Auffray et al. (2009) give a detailed analysis of this issue. We provide here a very brief description of their conclusions.

Let us consider an isometry of the (x_1, x_2) plane, $\boldsymbol{P}$: ${}^t\boldsymbol{P} \cdot \boldsymbol{P} = \boldsymbol{\delta}$. The transformation of $\mathbb{f}$ by $\boldsymbol{P}$, $\mathbb{f}^*$ is given by:

$$\mathbb{f}^*_{\alpha\beta\gamma\delta\epsilon\zeta} = P_{\alpha\eta}P_{\beta\theta}P_{\gamma\iota}P_{\delta\kappa}P_{\epsilon\lambda}P_{\zeta\mu}\mathbb{f}_{\eta\theta\iota\kappa\lambda\mu} \tag{9}$$

It can be rewritten with Voigt notation as:

$$[\mathbb{f}]^* = \hat{\boldsymbol{P}} \cdot [\mathbb{f}] \cdot {}^t\hat{\boldsymbol{P}} \tag{10}$$

where $\hat{\boldsymbol{P}}$ is a 6×6 matrix which components are explicitly known in terms of the components of $\boldsymbol{P}$. For a rotation, $\boldsymbol{P}^r = \left(\begin{smallmatrix} \cos\theta & -\sin\theta \\ \sin\theta & \cos\theta \end{smallmatrix}\right)$, and $\hat{\boldsymbol{P}}^r$ is the 6×6 matrix:

$$\hat{\boldsymbol{P}}^r = \begin{pmatrix} c^3 & cs^2 & -\sqrt{2}c^2s & -c^2s & -s^3 & \sqrt{2}cs^2 \\ cs^2 & c^3 & \sqrt{2}c^2s & -s^3 & -c^2s & -\sqrt{2}cs^2 \\ \sqrt{2}c^2s & -\sqrt{2}c^2s & (c^2-s^2)c & -\sqrt{2}cs^2 & \sqrt{2}cs^2 & -(c^2-s^2)s \\ c^2s & s^3 & -\sqrt{2}cs^2 & c^3 & cs^2 & -\sqrt{2}c^2s \\ s^3 & c^2s & \sqrt{2}cs^2 & cs^2 & c^3 & \sqrt{2}c^2s \\ \sqrt{2}cs^2 & -\sqrt{2}cs^2 & (c^2-s^2)s & \sqrt{2}c^2s & -\sqrt{2}c^2s & (c^2-s^2)c \end{pmatrix}$$

where c and s stand respectively for $\cos\theta$ and $\sin\theta$. When $\boldsymbol{P}$ is a reflection through $\boldsymbol{e}_2$ normal plane, $\boldsymbol{P}^m = \left(\begin{smallmatrix} 1 & 0 \\ 0 & -1 \end{smallmatrix}\right)$ and we have:

$$\hat{\boldsymbol{P}}^m = \begin{pmatrix} 1 & 0 & 0 & 0 & 0 & 0 \\ 0 & 1 & 0 & 0 & 0 & 0 \\ 0 & 0 & -1 & 0 & 0 & 0 \\ 0 & 0 & 0 & -1 & 0 & 0 \\ 0 & 0 & 0 & 0 & -1 & 0 \\ 0 & 0 & 0 & 0 & 0 & 1 \end{pmatrix}$$

If the laminated plate is invariant with respect to an isometry $\boldsymbol{P}$, then we have the following 21 linearly dependent equations:

$$[\mathbb{f}] = \hat{\boldsymbol{P}} \cdot [\mathbb{f}] \cdot {}^t\hat{\boldsymbol{P}}$$

Isotropy. A plate configuration is isotropic if its constitutive equation is both invariant by any planar rotation ($\hat{\boldsymbol{P}}^r$) and reflection ($\hat{\boldsymbol{P}}^m$). With this assumption, four independent constants still remain ($\mathbb{f}_{11}, \mathbb{f}_{12}, \mathbb{f}_{22}, \mathbb{f}_{26}$) and $\mathbb{f}$ is positive definite:

$$[\mathbb{f}] = \begin{pmatrix} \mathbb{f}_{11} & \mathbb{f}_{12} & 0 & 0 & 0 & \frac{\mathbb{f}_{11}-\mathbb{f}_{22}}{\sqrt{2}} - \mathbb{f}_{26} \\ \mathbb{f}_{12} & \mathbb{f}_{22} & 0 & 0 & 0 & \mathbb{f}_{26} \\ 0 & 0 & \frac{\mathbb{f}_{11}+\mathbb{f}_{22}}{2} - \mathbb{f}_{12} & \mathbb{f}_{26} & \frac{\mathbb{f}_{11}-\mathbb{f}_{22}}{\sqrt{2}} - \mathbb{f}_{26} & 0 \\ 0 & 0 & \mathbb{f}_{26} & \mathbb{f}_{22} & \mathbb{f}_{12} & 0 \\ 0 & 0 & \frac{\mathbb{f}_{11}-\mathbb{f}_{22}}{\sqrt{2}} - \mathbb{f}_{26} & \mathbb{f}_{12} & \mathbb{f}_{11} & 0 \\ \frac{\mathbb{f}_{11}-\mathbb{f}_{22}}{\sqrt{2}} - \mathbb{f}_{26} & \mathbb{f}_{26} & 0 & 0 & 0 & \frac{\mathbb{f}_{11}+\mathbb{f}_{22}}{2} - \mathbb{f}_{12} \end{pmatrix} \tag{11}$$

It is possible to simplify further this constitutive equation when a laminate is a stack of plies with different isotropic constitutive materials (this symmetry is also valid for some functionally graded materials (Nguyen et al., 2008a,b)). We use the spectral decomposition of plane stress stiffness:

$$\boldsymbol{c}(x_3) = \frac{2\nu(x_3)E(x_3)}{1-\nu^2(x_3)}\boldsymbol{j} + \frac{E(x_3)}{1+\nu(x_3)}\boldsymbol{i}$$

where E is the Young modulus, ν Poisson's ratio and $j_{\alpha\beta\gamma\delta} = 1/2\delta_{\alpha\beta}\delta_{\gamma\delta}$. Deriving directly the constitutive equation (29) with this decomposition enables us to demonstrate that $\mathbb{f}_{26} = -\mathbb{f}_{12}$. Three independent constants $\mathbb{f}_{11}, \mathbb{f}_{12}, \mathbb{f}_{22}$ still remain and $\mathbf{f}$ is no more invertible:

$$\mathbf{f} = (\mathbb{f}_{11} + \mathbb{f}_{22} + 2\mathbb{f}_{12})\, \boldsymbol{i}\cdot\boldsymbol{i} - 2\,(\mathbb{f}_{22} + \mathbb{f}_{12})\left(\boldsymbol{j}\cdot\boldsymbol{i} + \boldsymbol{i}\cdot\boldsymbol{j}\right) + \mathbb{f}_{22}\boldsymbol{j}\cdot\boldsymbol{j} \tag{12}$$

Finally, for a plate with a homogeneous and isotropic constitutive material, we have demonstrated that the Bending-Gradient model is turned into a Reissner-Mindlin plate model and that $\mathbf{f} = \frac{6}{5Gh}\boldsymbol{i}\cdot\boldsymbol{i}$ in Part I. This is rewritten as

$$[\mathbf{f}] = \frac{6}{5Gh}\begin{pmatrix} 1 & 0 & 0 & 0 & 0 & 1/\sqrt{2} \\ 0 & 0 & 0 & 0 & 0 & 0 \\ 0 & 0 & 1/2 & 0 & 1/\sqrt{2} & 0 \\ 0 & 0 & 0 & 0 & 0 & 0 \\ 0 & 0 & 1/\sqrt{2} & 0 & 1 & 0 \\ 1/\sqrt{2} & 0 & 0 & 0 & 0 & 1/2 \end{pmatrix} \tag{13}$$

In this case: $\mathbb{f}_{11} = \frac{6}{5Gh}$ and $\mathbb{f}_{12} = \mathbb{f}_{22} = 0$ which is different from the general case of a layered plate made of different isotropic constitutive materials (Equation 12). Consequently, even for these laminates, the Bending-Gradient model is *a priori* not a Reissner-Mindlin model. This is mainly because the different Poisson's ratios in each layer generates warping. When Poisson's ratio is uniform through the thickness, the constitutive equation is such that $\mathbb{f}_{12} = \mathbb{f}_{22} = 0$ and for conventional isotropic materials, the warping effect remains very limited, leading to a quasi homogeneous constitutive equation.

4. Closed-form solution for Pagano's configuration

4.1. Plate closed-form solution

Pagano (1969) gives an exact solution for cylindrical bending of simply supported composite laminates. We choose the same configuration for the Bending-Gradient model. The plate is invariant and infinite in x_2 direction. It is out-of-plane loaded with $p_3(x_1) = -p_0 \sin \kappa x_1$ where $\lambda = 1/\kappa = \frac{L}{n\pi}$, $n \in \mathbb{N}^{+*}$ is the wavelength of the loading (Figure 2).

The plate is simply supported at $x_1 = 0$ and $x_1 = L$ with traction free edges:

$$U_3(0) = 0, \quad U_3(L) = 0, \quad \boldsymbol{M}(0) = \mathbf{o}, \quad \boldsymbol{M}(L) = \mathbf{o}, \quad \boldsymbol{N}(0)\cdot\boldsymbol{e}_1 = \mathbf{o}, \quad \boldsymbol{N}(L)\cdot\boldsymbol{e}_1 = \mathbf{o} \tag{14}$$

In these boundary conditions, $M_{22}(0) = M_{22}(L) = 0$ is the additional boundary condition compared to the Reissner-Mindlin plate model. This boundary condition is very similar to the one which applies to the bimoment on a free section in Vlasov (1961) beam theory. This additional boundary condition takes into account free edge effects similar to those described in Lebée and Sab (2010b) for periodically layered laminate.

The solution is obtained as follows: First, the x_2-invariance leads to several simplifications and some unknowns vanish. Second, relevant equations and unknowns are gathered into a differential system and the closed-form solution is derived.

4.1.1. Simplifications related to x_2-invariance

Membrane solution. Since $(\boldsymbol{N}, \boldsymbol{M})$ fields are uncoupled from shear fields, it is possible to solve separately the membrane part of the plate model. Hence, the x_2-invariance in the membrane strain definition (3a) enforces $e_{22} = U_{2,2} = 0$. Moreover, boundary conditions (2d) and equilibrium equation (2a) for membrane stresses lead easily to $N_{11} = N_{12} = 0$. However, N_{22}, e_{11} and e_{12} remain undetermined.

Curvatures. Curvatures are defined by Equation 3b: $\chi_{\alpha\beta} = \Phi_{\alpha\beta\gamma,\gamma}$. Taking into account x_2 invariance leads to:

$$[\boldsymbol{\chi}] = \begin{pmatrix} \chi_{11} \\ \chi_{22} \\ \sqrt{2}\chi_{12} \end{pmatrix} = \begin{pmatrix} \Phi_{111,1} \\ \Phi_{221,1} \\ \sqrt{2}\Phi_{121,1} \end{pmatrix} = \begin{pmatrix} \Phi_{1,1} \\ \Phi_{2,1} \\ \Phi_{3,1} \end{pmatrix} \tag{15}$$

Kirchhoff-Love constitutive equation. Kirchhoff-Love constitutive equations (4a) and (4b) are written with Voigt notation in the inverse form as:

$$[e] = [a] \cdot [N] + [b] \cdot [M] \tag{16a}$$

$$[\chi] = {}^{t}[b] \cdot [N] + [d] \cdot [M] \tag{16b}$$

where $[a]$, $[b]$ and $[d]$ are Kirchhoff-Love compliance matrices.

Taking into account $N_{11} = N_{12} = 0$ and $e_{22} = 0$ enables us to rewrite Kirchhoff-Love constitutive equation in a compact form as:

$$[\chi] = [d]^{*} \cdot [M] \tag{17}$$

where

$$d^{*}_{ij} = d_{ij} - \frac{b_{2i} b_{2j}}{a_{22}}$$

is the effective flexural stiffness taking into account $e_{22} = 0$ constraint. N_{22}, e_{11} and e_{12} are then derived directly from the bending moment using equations:

$$e_i = \left(b_{ij} - \frac{a_{i2} b_{2j}}{a_{22}} \right) M_j \quad \text{and} \quad N_2 = -\frac{b_{2i}}{a_{22}} M_i \tag{18}$$

Equilibrium. The x_2 invariance in the bending gradient equilibrium equation (2b) enforces:

$$\begin{pmatrix} \mathtt{R}_1 \\ \mathtt{R}_2 \\ \mathtt{R}_3 \\ \mathtt{R}_4 \\ \mathtt{R}_5 \\ \mathtt{R}_6 \end{pmatrix} = \begin{pmatrix} M_{11,1} \\ M_{22,1} \\ \sqrt{2} M_{12,1} \\ 0 \\ 0 \\ 0 \end{pmatrix} \tag{19}$$

and transverse loading equilibrium equation (2c) becomes:

$$M_{11,11} = -p_3(x_1) \tag{20}$$

Shear constitutive equation. Taking into account $\mathtt{R}_4 = \mathtt{R}_5 = \mathtt{R}_6 = 0$, $U_{3,2} = 0$ and generalized shear strain definition (3c), Shear constitutive equation (4c) is rewritten in two parts.

A first part with unknowns involving active boundary conditions:

$$\begin{pmatrix} \Phi_1 \\ \Phi_2 \\ \Phi_3 \end{pmatrix} = \begin{pmatrix} \mathtt{f}_{11} & \mathtt{f}_{12} & \mathtt{f}_{13} \\ \mathtt{f}_{12} & \mathtt{f}_{22} & \mathtt{f}_{23} \\ \mathtt{f}_{13} & \mathtt{f}_{23} & \mathtt{f}_{33} \end{pmatrix} \cdot \begin{pmatrix} M_{11,1} \\ M_{22,1} \\ \sqrt{2} M_{12,1} \end{pmatrix} - \begin{pmatrix} U_{3,1} \\ 0 \\ 0 \end{pmatrix} \tag{21}$$

and a second part which enables the derivation of Φ_4, Φ_5, Φ_6 on which no boundary condition applies:

$$\begin{pmatrix} \Phi_4 \\ \Phi_5 \\ \Phi_6 \end{pmatrix} = \begin{pmatrix} \mathtt{f}_{41} & \mathtt{f}_{42} & \mathtt{f}_{43} \\ \mathtt{f}_{51} & \mathtt{f}_{52} & \mathtt{f}_{53} \\ \mathtt{f}_{61} & \mathtt{f}_{62} & \mathtt{f}_{63} \end{pmatrix} \cdot \begin{pmatrix} M_{11,1} \\ M_{22,1} \\ \sqrt{2} M_{12,1} \end{pmatrix} - \begin{pmatrix} 0 \\ 0 \\ U_{3,1}/\sqrt{2} \end{pmatrix} \tag{22}$$

4.1.2. Resolution

Final System. Finally, combining Equations 14, 15, 17, 20 and 21, leads to the following set of equations which fully determines the problem:

$$\begin{cases} M_{11,11} = p_0 \sin \kappa x_1 & \text{(23a)} \\ [d]^{*} \cdot [M] - \tilde{f} \cdot [M]_{,11} = \begin{pmatrix} U_{3,11} \\ 0 \\ 0 \end{pmatrix} & \text{(23b)} \\ [M] = 0 \quad \text{for} \quad x_1 = 0 \quad \text{and} \quad x_1 = L & \text{(23c)} \\ U_3 = 0 \quad \text{for} \quad x_1 = 0 \quad \text{and} \quad x_1 = L & \text{(23d)} \end{cases}$$

where for convenience, $\tilde{\boldsymbol{f}}$ is the 3×3 submatrix of $[\mathbb{f}]$:

$$\tilde{\boldsymbol{f}} = \begin{pmatrix} \mathbb{f}_{11} & \mathbb{f}_{12} & \mathbb{f}_{13} \\ \mathbb{f}_{12} & \mathbb{f}_{22} & \mathbb{f}_{23} \\ \mathbb{f}_{13} & \mathbb{f}_{23} & \mathbb{f}_{33} \end{pmatrix}$$

Once $[\boldsymbol{M}]$ is derived, the non-zero unknowns are derived using Equations 18, 19 and 22.

Solution. Since $\tilde{\boldsymbol{f}}$ is positive and $[\boldsymbol{d}]^*$ is positive definite, the differential system 23 is well-posed and the solution is the sum of a particular solution and hyperbolic solutions of the homogeneous equation. Boundary conditions applied to $\boldsymbol{M}$ vanish hyperbolic solutions. There remains the particular solution:

$$[\boldsymbol{M}] = \begin{pmatrix} -1 \\ \boldsymbol{g}^{-1} \cdot \boldsymbol{g} \end{pmatrix} p_0 \lambda^2 \sin \kappa x_1 \quad \text{and} \quad U_3 = -p_0 \lambda^4 \left(g_{11} - {}^t\boldsymbol{g} \cdot \boldsymbol{g}^{-1} \cdot \boldsymbol{g} \right) \sin \kappa x_1 \tag{24}$$

where

$$\tilde{\boldsymbol{g}} = [\boldsymbol{d}]^* + \kappa^2 \tilde{\boldsymbol{f}}, \quad \boldsymbol{g} = \begin{pmatrix} g_{22} & g_{23} \\ g_{23} & g_{33} \end{pmatrix}, \quad \boldsymbol{g} = \begin{pmatrix} g_{12} \\ g_{13} \end{pmatrix}. \tag{25}$$

The matrix $\tilde{\boldsymbol{g}}$ appears to be the effective flexural stiffness for cylindrical bending, corrected with shear effects. When $\kappa \to 0$, $\tilde{\boldsymbol{g}} = \tilde{\boldsymbol{d}}^*$ which yields exactly the Kirchhoff-Love solution.

4.2. Localization

Once the generalized stresses are derived, it is possible to reconstruct local 3D fields, using the localization procedure described in Part I. The local 3D stress $\tilde{\boldsymbol{\sigma}}^{BG}$ is the sum of three terms depending linearly on the generalized stresses:

$$\tilde{\boldsymbol{\sigma}}^{BG} = \tilde{\boldsymbol{s}}^{(N)} : \boldsymbol{N} + \tilde{\boldsymbol{s}}^{(M)} : \boldsymbol{M} + \tilde{\boldsymbol{s}}^{(\mathbb{R})} \therefore \mathbf{R} \tag{26}$$

where,

$$\begin{cases} s^{(N)}_{\alpha\beta\epsilon\zeta}(x_3) = c_{\alpha\beta\gamma\delta}(x_3) \left(a_{\delta\gamma\epsilon\zeta} + x_3 \, b_{\zeta\epsilon\gamma\delta} \right) \quad \text{and } s^{(N)}_{i3\epsilon\zeta} = 0 & \text{(27a)} \\ s^{(M)}_{\alpha\beta\epsilon\zeta}(x_3) = c_{\alpha\beta\gamma\delta}(x_3) \left(b_{\delta\gamma\epsilon\zeta} + x_3 \, d_{\delta\gamma\epsilon\zeta} \right) \quad \text{and } s^{(M)}_{i3\epsilon\zeta} = 0 & \text{(27b)} \\ s^{(\mathbb{R})}_{\alpha 3\eta\zeta\epsilon}(x_3) = -\displaystyle\int_{-\frac{h}{2}}^{x_3} c_{\alpha\eta\gamma\delta}(z) \left(b_{\delta\gamma\epsilon\zeta} + z \, d_{\delta\gamma\epsilon\zeta} \right) dz \ , \ s^{(\mathbb{R})}_{\alpha\beta\eta\zeta\epsilon} = 0 \text{ and } s^{(\mathbb{R})}_{33\eta\zeta\epsilon} = 0 & \text{(27c)} \end{cases}$$

and $\boldsymbol{c}(x_3)$ is the local plane-stress stiffness tensor.

It is possible to rewrite Equation 26 with Voigt notations as follows:

$$\tilde{\boldsymbol{\sigma}}^{BG,\backslash\backslash} = \begin{pmatrix} \sigma^{BG}_{11} \\ \sigma^{BG}_{22} \\ \sqrt{2}\sigma^{BG}_{12} \end{pmatrix} = \tilde{\mathbf{s}}^{(N)} \cdot [\boldsymbol{N}] + \tilde{\mathbf{s}}^{(M)} \cdot [\boldsymbol{M}]$$

$$\boldsymbol{\sigma}^{BG,\perp} = \begin{pmatrix} \sigma^{BG}_{13} \\ \sigma^{BG}_{23} \end{pmatrix} = \overline{\mathbf{s}}^{(\mathbb{R})} \cdot [\mathbf{R}]$$

where

$$\tilde{\mathbf{s}}^{(N)}(x_3) = [\boldsymbol{c}]\,(x_3) \cdot \left([\boldsymbol{a}] + x_3{}^t[\boldsymbol{b}] \right)$$

$$\tilde{\mathbf{s}}^{(M)}(x_3) = [\boldsymbol{c}]\,(x_3) \cdot ([\boldsymbol{b}] + x_3[\boldsymbol{d}])$$

$$\overline{\mathbf{s}}^{(\mathbb{R})}(x_3) = -\int_{-\frac{h}{2}}^{x_3} [\![\boldsymbol{c}(z) : (\boldsymbol{b} + z\,\boldsymbol{d})]\!] dz$$

$\tilde{\boldsymbol{s}}^{(N)}$ and $\tilde{\boldsymbol{s}}^{(M)}$ are 3×3 matrices and $\overline{\boldsymbol{s}}^{(\mathbb{R})}$ is a 2×6 matrix. Straight double stroked brackets $[\![\bullet]\!]$ denote here the following matrix representation of a fourth-order tensor:

$$[\![\mathcal{L}]\!] = \begin{pmatrix} \mathcal{L}_{1111} & \mathcal{L}_{1122} & \sqrt{2}\mathcal{L}_{1121} & \mathcal{L}_{1211} & \mathcal{L}_{1222} & \sqrt{2}\mathcal{L}_{1221} \\ \mathcal{L}_{2111} & \mathcal{L}_{2122} & \sqrt{2}\mathcal{L}_{2121} & \mathcal{L}_{2211} & \mathcal{L}_{2222} & \sqrt{2}\mathcal{L}_{2221} \end{pmatrix} \tag{28}$$

This reallocation is also useful for the derivation of the shear compliance tensor derived in Part I:

$$[\mathbb{f}] = \int_{-\frac{h}{2}}^{\frac{h}{2}} \left(\int_{-\frac{h}{2}}^{x_3} {}^{t}[\![\boldsymbol{c}(z) : (\boldsymbol{\mathcal{b}} + z\,\boldsymbol{\mathcal{d}})]\!] dz \right) \cdot \boldsymbol{S}(x_3) \cdot \left(\int_{-\frac{h}{2}}^{x_3} [\![\boldsymbol{c}(z) : (\boldsymbol{\mathcal{b}} + z\,\boldsymbol{\mathcal{d}})]\!] dz \right) dx_3 \tag{29}$$

where $S_{\alpha\beta}(x_3) = 4\mathcal{S}_{\alpha 3\beta 3}(x_3)$ is the out-of-plane shear compliance tensor.

Since $\mathbb{f}$ is not always invertible, we introduce Moore-Penrose pseudo inverse for the shear stiffness tensor $\mathbb{F}$:

$$\mathbb{F} = \lim_{\kappa\to 0} \left(\mathbb{f} \therefore \mathbb{f} + \kappa \mathbb{I}\right)^{-1} \therefore \mathbb{f}$$

which is used in the constraint on generalized shear strain $\boldsymbol{\Gamma}$ in Equation 4c.

Finally, the in-plane displacement localization was suggested in Part I as:

$$\boldsymbol{u}^{BG} = \boldsymbol{U} - x_3 \boldsymbol{\nabla} U_3 + \boldsymbol{v}^{(\mathbb{R})} \therefore \mathbb{R} \tag{30}$$

where

$$v_\alpha^{(\mathbb{R})} = \left(\int_{-\frac{h}{2}}^{x_3} S_{\alpha\zeta}(z) s^{(\mathbb{R})}_{\zeta 3\beta\gamma\delta}(z) dz + \mathcal{k}^{(\mathbb{R})}_{\alpha\beta\gamma\delta} \right) \tag{31}$$

and $\boldsymbol{\mathcal{k}}^{(\mathbb{R})}$ is chosen such as $\left\langle u_\alpha^{(\mathbb{R})} \right\rangle = 0$. This is rewritten with Voigt notation as:

$$\boldsymbol{u}^{BG} = \boldsymbol{U} - x_3 \boldsymbol{\nabla} U_3 + \overline{\boldsymbol{v}}^{(\mathbb{R})} \cdot [\mathbb{R}]$$

where

$$\overline{\boldsymbol{v}}^{(\mathbb{R})}(x_3) = -\int_{-\frac{h}{2}}^{x_3} \boldsymbol{S}(z) \cdot \int_{-\frac{h}{2}}^{z} [\![\boldsymbol{c}(u) : (\boldsymbol{\mathcal{b}} + u\,\boldsymbol{\mathcal{d}})]\!] du dz + [\![\boldsymbol{\mathcal{k}}^{(\mathbb{R})}]\!]$$

4.3. Application to laminates

4.3.1. Plate configuration

We consider angle-ply laminates. Each ply is made of unidirectional fiber-reinforced material oriented at θ relative to the bending direction x_1. All plies have the same thickness and are perfectly bounded. A laminate is denoted between brackets by the successive ply-orientations along the thickness. For instance $[0°, 90°]$ denotes a 2-ply laminate where the lower ply fibers are oriented in the bending direction. When the laminate follows mirror symmetry described in Section 3.3, only half of the stack is given and the subscript s is added. Thus $[30°, -30°]_s$ means $[30°, -30°, -30°, 30°]$.

The constitutive behavior of a ply is assumed to be transversely isotropic along the direction of the fibers and engineering constants are chosen similar to those of Pagano (1969):

$$E_L = 25\times 10^6 psi, \quad E_T = E_N = 1\times 10^6 psi, \quad G_{LT} = G_{LN} = 0.5\times 10^6 psi,$$

$$G_{NT} = \frac{E_T}{2(1+\nu_{NT})} = 0.4\times 10^6 psi, \quad \nu_{LT} = \nu_{LN} = \nu_{NT} = 0.25$$

where G_{NT} has been changed to preserve transversely isotropic symmetry. L is the longitudinal direction oriented in the (x_1, x_2) plane at θ with respect to $\tilde{\boldsymbol{e}}_1$, T is the transverse direction and N is the normal direction coinciding with $\tilde{\boldsymbol{e}}_3$.

Pagano (1969, 1970a,b) derived exact 3D elasticity solution of this problem for a laminate loaded only on the upper face and free on the lower face. In the present work we assume the plate is identically loaded on its upper and lower face to comply with the plate model: $T_3^+ = T_3^- = \frac{p_3}{2}$ where $T_3^\pm$ is the normal traction on the upper and lower face of the plate.

4.3.2. Localization fields

Shear forces are related to the bending gradient as follows: $Q_1 = \mathtt{R}_{111} + \mathtt{R}_{122}$ and $Q_2 = \mathtt{R}_{121} + \mathtt{R}_{222}$. Thus we suggested in Part I the following signification for the bending gradient components:

$\mathtt{R}_{111} - \mathtt{R}_1$: Cylindrical Bending part of Q_1
$\mathtt{R}_{221} - \mathtt{R}_2$: Pure warping
$\mathtt{R}_{121} - \mathtt{R}_3$: Torsional part of Q_2
$\mathtt{R}_{112} - \mathtt{R}_4$: Pure warping
$\mathtt{R}_{222} - \mathtt{R}_5$: Cylindrical Bending part of Q_2
$\mathtt{R}_{122} - \mathtt{R}_6$: Torsional part of Q_1

In Figure 3 are plotted localization shear stress distributions $\overline{\boldsymbol{s}}^{(\mathtt{R})}$ derived in Section 4.2 corresponding to each components of $\mathbf{R}$ in both directions for a quasi-isotropic laminate $[0°, -45°, 90°, 45°]_s$. All stress distributions are continuous and fulfill traction free boundary conditions on the upper and lower faces of the plate. For each direction there are four self-equilibrated stress distribution ($\langle \sigma_{\alpha 3} \rangle = 0$) associated to $\mathtt{R}_2, \mathtt{R}_3, \mathtt{R}_4$ and $\mathtt{R}_5$ for Direction 1 and $\mathtt{R}_1, \mathtt{R}_2, \mathtt{R}_4$ and $\mathtt{R}_6$ for Direction 2. This explains the suggested signification for shear variables. We draw the reader's attention to the fact that, even if there are self-equilibrated stress distributions, all distributions have comparable amplitude and none can be neglected at this stage. Moreover, it is clear that torsion generates different distributions than pure cylindrical bending, except in the homogeneous case.

4.3.3. Distance between the Reissner-Mindlin and the Bending-Gradient model

In Part I we introduced the relative distance between the Bending-Gradient model and a Reissner-Mindlin model, $\Delta^{RM/BG}$:

$$\Delta^{RM/BG} = \frac{\|\mathbf{f}^{\mathrm{W}}\|}{\|\mathbf{f}^{RM}\|} \tag{32}$$

where

$$\|\mathbf{f}\| = \sqrt{{}^t[\mathbf{f}] : [\mathbf{f}]} \tag{33}$$

is the norm for Bending-Gradient compliance tensors and $\mathbf{f}^{\mathrm{W}}$ is the pure warping part of $\mathbf{f}$:

$$[\mathbf{f}]^{\mathrm{W}} = [\mathbf{f}] - \frac{4}{9}{}^t[\![\boldsymbol{i}]\!] \cdot [\![\boldsymbol{i}]\!] \cdot [\mathbf{f}] \cdot {}^t[\![\boldsymbol{i}]\!] \cdot [\![\boldsymbol{i}]\!] \tag{34}$$

$\Delta^{RM/BG}$ gives an estimate of the pure warping fraction of the shear stress energy. When the plate constitutive equation is restricted to a Reissner-Mindlin one we have exactly $\Delta^{RM/BG} = 0$.

In Table 1, are given the values of $\Delta^{RM/BG}$ for the laminates considered in this work. For a single ply, the criterion is zero since in Part I we demonstrated that the Bending-Gradient model is exactly a Reissner-Mindlin model in this case. However, when there are several plies, the distance can be greater than 10%. Thus with these laminates, the shear constitutive equation cannot be reduced to a Reissner-Mindlin behavior.

Stack	$[0°]$	$[0°, 90°]$	$[0°, 90°, 0°, 90°, 0°, 90°, 0°, 90°, 0°]$	$[0°, -45°, 90°, 45°]_s$
$\Delta^{RM/BG}$	0	16.0%	4.63%	12.4%

Table 1: The criterion $\Delta^{RM/BG}$ for several laminates

5. Comparison with other single equivalent layer approaches

5.1. Other single equivalent layer approaches

5.1.1. The Reissner-Mindlin model with the approach from Whitney (1972)

Closed-form solutions using the Reissner-Mindlin model were derived in order to compare them with the Bending-Gradient. The resolution of the cylindrical bending problem is quite similar so it will not be detailed here. The work of Whitney (1972) was used for deriving transverse shear stress distributions and shear correction factors were taken into account into the shear constitutive equation of the Reissner-Mindlin plate model.

Let us recall briefly the method. Whitney (1972) assumes the plate is under cylindrical bending: $\boldsymbol{Q}_1 = \boldsymbol{M}_{11,1}$, $\boldsymbol{Q}_2 = \boldsymbol{M}_{12,1}$, $\boldsymbol{e}_{22} = 0$ and $\boldsymbol{\chi}_{22} = 0$ and derives transverse shear distribution $\tilde{\boldsymbol{\sigma}}^{(Q),W}(x_3)$ following a procedure almost identical to the one proposed in Part I. Then he computes the shear correction factor defined as:

$$k_1^2 = \frac{f_{11}^{FSDT}}{\left\langle \tilde{\boldsymbol{\sigma}}^{Q_1} : \tilde{\boldsymbol{\mathcal{S}}}(x_3) : \tilde{\boldsymbol{\sigma}}^{Q_1} \right\rangle}$$

where f_{11}^{FSDT} is the First Order Shear Deformation Theory shear compliance: $\boldsymbol{f}^{FSDT} = \left(\boldsymbol{F}^{FSDT}\right)^{-1}$ where $F_{\alpha\beta}^{FSDT} = \langle \mathcal{C}_{\alpha 3 \beta 3}(x_3) \rangle$. The shear correction factor in the second direction k_2 is derived in the same way while rotating the plate of $\pi/2$. Once shear correction factors are derived, the corrected shear stiffness $\boldsymbol{F}^{RM,W}$ is defined as follows:

$$\boldsymbol{F}^{RM,W} = \boldsymbol{k} \cdot \boldsymbol{F}^{FSDT} \cdot \boldsymbol{k} \tag{35}$$

where $\boldsymbol{k} = \left(\begin{smallmatrix} k_1 & 0 \\ 0 & k_2 \end{smallmatrix}\right)$

5.1.2. Finite element analysis

A comparison with a finite elements solution was also performed on ABAQUS (2007). Since the Bending-Gradient is an Equivalent Single Layer theory, conventional shell elements were chosen (3 displacements and 3 rotations). Transverse shear fields with conventional shell elements in ABAQUS are derived using an approach very similar to Whitney (1972) where it is furthermore assumed that the plate overall constitutive equation is orthotropic with respect to the main bending direction. $S4$, linear quadrangle with full integration elements, were used. A convergence test was performed comparing the FE mid-span deflection $U^{RM,FE}$ to the exact solution from Pagano (1969) U^{Ex} which ensures that the FE error increment is 1/1000 of the error with the exact solution $((U^{RM,FE} - U^{Ex})/U^{Ex})$. This study enforced the typical size of an element $l_{char} = h/5$ where h is the plate thickness. For instance when the slenderness is $L/h = 4$ there are 20 elements. Figure 4 shows a typical deformation of this mesh. Periodicity was enforced on lateral edges of the strip in Figure 4 by equating corresponding rotations and displacements. Finally 61 section points were required as output and section integration is performed during the analysis. The number of section points is only an output parameter and has no incidence on the convergence.

5.2. Error estimates

Two error estimates are introduced: the first one for the transverse shear part of the stresses for which we introduce the following seminorm:

$$\|\boldsymbol{\sigma}\|^2 = \int_0^L \int_{-\frac{h}{2}}^{\frac{h}{2}} \sigma_{\alpha 3} \mathcal{S}_{\alpha 3 \beta 3} \sigma_{\beta 3} dx_3 dx_1$$

and we define the relative error as:

$$\Delta(\boldsymbol{\sigma}) = \frac{\|\boldsymbol{\sigma}^{Ex} - \boldsymbol{\sigma}\|}{\|\boldsymbol{\sigma}^{Ex}\|}$$

where $\boldsymbol{\sigma}^{Ex}$ is the exact shear stress distribution from Pagano (1969, 1970a,b). The second one is the mid-span deflection relative error:

$$\Delta(U_3) = \frac{U_3^{Ex}(L/2) - U_3(L/2)}{U_3^{Ex}(L/2)}$$

where $U_3^{Ex}(x_1) = \frac{\langle u_3^{Ex}(x_3)\rangle}{h}$ is the plate deflection taken for the exact solution.

5.3. Results

5.3.1. $[0°, 90°, 0°, 90°, 0°, 90°, 0°, 90°, 0°]$ *ply*

In this section, we consider first a symmetric cross ply $[0°, 90°, 0°, 90°, 0°, 90°, 0°, 90°, 0°]$ laminate. In this case, the plate configuration fulfills the assumptions made for the finite elements approximation (orthotropic laminate). In Figure 5, shear stress distribution at $x_1 = 0$ in Direction 1 is plotted for the exact solution from Pagano (1969) $\boldsymbol{\sigma}^{Ex}$, the Bending-Gradient solution $\boldsymbol{\sigma}^{(\mathrm{R})}$, Whitney's shear distribution $\boldsymbol{\sigma}^{(Q),W}$ and the finite elements solution $\boldsymbol{\sigma}^{(Q),FE}$. The slenderness ratio is set to $L/h = 4$ as conventionally done when benchmarking plate models. The reader is referred to (Whitney, 1972; Noor and Malik, 2000; Yu et al., 2002; Nguyen et al., 2005; Carrera, 2003) among others. The three approximate solutions yield the same distribution. The discrepancy with the exact solution is well-known and associated to edge effects.

In Figure 6 is plotted the in-plane displacement at $x_1 = 0$ in Direction 1. The displacement is normalized with the mid-span Kirchhoff-Love deflection, U_3^{KL}. The Bending-Gradient approximation follows closely the exact solution.

In Figure 7 the transverse shear stress distribution error $\Delta(\boldsymbol{\sigma})$ versus the slenderness ratio L/h is plotted for the Bending-Gradient solution (BG), the finite elements solution (RM, FE) and the closed-form Reissner-Mindlin solution (RM, WE). In Figure 8 the mid-span deflection error is also plotted versus the slenderness ratio. Kirchhoff-Love deflection is also plotted as reference. The three approximate solutions yield almost the same error both for deflection and transverse shear stress and converge as $\Delta(\boldsymbol{\sigma}^{BG}) \propto \left(\frac{h}{L}\right)^2$ with the slenderness ratio.

5.3.2. $[0°, 90°]$ *ply*

We consider now a non-symmetric cross ply $[0°, 90°]$ laminate. The plate configuration still fulfills the assumptions made for the finite elements approximation. In Figure 9, shear stress distribution in Direction 1 is plotted. Again, the three approximate solutions yield the same distribution.

In Figure 10 is plotted the in-plane displacement in Direction 1. The Bending-Gradient approximation follows some trends of the exact solution. However, there is a small discrepancy with the exact solution.

In Figure 11 the transverse shear stress distribution error $\Delta(\boldsymbol{\sigma})$ versus the slenderness ratio L/h is plotted. In this case, Whitney's solution converges with L/h whereas finite elements and Bending-Gradient approximations do not converge and lead to small residual errors ($\simeq 10^{-3}$). In Figure 12 the mid-span deflection error is also plotted versus the slenderness ratio. Again the three approximate solutions yield almost the same error.

5.3.3. $[45°, -45°, 45°, -45°, 45°, -45°, 45°, -45°, 45°]$ *ply*

Now we take the initial 9-ply configuration and simply rotate it 45° with respect to the bending direction. It becomes a symmetric and non-orthotropic $[45°, -45°, 45°, -45°, 45°, -45°, 45°, -45°, 45°]$ laminate. This configuration does not comply with the assumptions made for the finite elements approach. In Figure 13 shear distributions are compared to the exact solution. The Bending-Gradient solution remains close to the exact solution. However finite elements and Whitney's solution yield a different distribution which is not as accurate as the Bending-Gradient. More precisely, in Direction 2, the FE solution does not capture the change of slope associated to the change of ply orientation.

In Figure 14 is plotted the in-plane displacement in both directions. The Bending-Gradient approximation matches accurately the exact solution. Especially, in Direction 2 the distribution follows a Zig-Zag shape. Thus the Bending-Gradient approximation is able to capture this well-known feature of laminates displacement fields.

In Figure 15 the transverse shear stress distribution error versus the slenderness ratio is plotted. Contrary to the finite elements solution and Whitney's solution, the Bending-Gradient solution converges when the plate is slender. In Figure 16 the mid-span deflection error is also plotted versus the slenderness ratio. The Bending-Gradient solution is the most accurate one for conventional slenderness.

5.3.4. $[45°, -45°]$ *ply*

Again we take the $[0°, 90°]$ ply and rotate it with respect to the bending direction. This lead to a non-symmetric and non-orthotropic ply $[45°, -45°]$ and this configuration does not comply with the assumptions made for the finite elements approach. The comparison is made in Figure 17 for transverse shear stress. The Bending-Gradient solution remains close to the exact solution and Whitney's solution yields acceptable results (except a mismatch for $\sigma_{23}^{(Q),W}$). However in this case, finite elements yields inappropriate results: in Direction 1 the stress distribution does not respect macroscopic equilibrium $\left\langle \sigma_{13}^{FE} \right\rangle \neq Q_1$. We checked nevertheless that FE nodal forces fulfills macroscopic equilibrium.

In Figure 18 is plotted the in-plane displacement in both directions. The Bending-Gradient approximation matches accurately the exact solution in Direction 1. In Direction 2 there is an offset between the Bending-Gradient approximation and the exact solution, however the overall shape of the displacement is captured.

The inaccuracy of finite element and Whitney's solutions is again clear in Figure 19 showing the transverse shear stress distribution error versus the slenderness ratio whereas the Bending-Gradient converges as $\Delta(\boldsymbol{\sigma}^{BG}) \propto \left(\frac{h}{L}\right)^2$ and both the Whitney and finite elements solutions lead to non negligible errors. Again, in Figure 20, the deflection error indicates that FE are too compliant and that the Bending-Gradient is more accurate than the Reissner-Mindlin solution.

5.3.5. Influence of the bending direction

As already mentioned, the finite elements approach makes assumption on the overall plate configuration (orthotropy). However, in standard engineering application, even if the plate is orthotropic, the bending direction does not often correspond to the orthotropy axis. In order to illustrate this, we consider here the cross ply $[0°, 90°]$ laminate with fixed slenderness $L/h = 4$ and we rotate the bending directions (the plate's overall configuration is rotating relative to x_3 axis). In Figure 21 we plotted the deflection error with respect to the bending direction for the different approximations. It is clear that the bending direction has a great influence on the accuracy of the deflection. Even for the Reissner-Mindlin approximation, the error can be four times greater than the error for the Bending-Gradient.

5.4. Discussion

We have numerically compared three approaches for deriving an approximation of the exact solution for cylindrical bending suggested by Pagano (1969, 1970a,b) applied to two cross-ply configurations (one mirror-symmetric and one non-symmetric) and in two bending directions.

The first main observation which comes out of this analysis is the critical influence of the assumption of orthotropy with respect to the bending direction. When this assumption is fullfilled, the three approximations lead to almost identical results. Otherwise, both Whitney's and Finite Element approximations lead to poor estimation of transverse shear stress distribution and deflection. In the case of finite elements this is because we do not respect the assumption of the model. In the case of Whitney (1972), the main reason for this discrepancy comes from the assumption of cylindrical bending. This assumption neglects the influence of the pure warping unknowns included in the bending gradient: $\mathtt{R}_{112}$ and $\mathtt{R}_{221}$ and generates the difference in shear stress distribution and therefore in deflection.

The second observation is that a simple rotation of the plate with respect to the bending direction leads to very different transverse shear stress distribution. This shows clearly the necessity to distinguish between torsion and cylindrical bending components in the gradient of the bending moment. In most plate models they are mixed into shear forces ($Q_1 = \mathtt{R}_{111} + \mathtt{R}_{122}$), whereas, as illustrated in Section 4.3.2, the components $\mathtt{R}_{111}$ and $\mathtt{R}_{122}$ lead to different transverse shear stress distributions. This explains the significant difference when changing the bending direction. More generally, this raises the question of the relevence

of benchmarking plate models in configurations where only the cylindrical part of the bending gradient is involved whereas laminated plate engineering applications involves much more general configurations.

Finally, the Bending-Gradient solution was presented. When the plate follows mirror symmetry, this model gives a very good approximation of both local and macroscopic fields at a rather low computational cost (no post-process integration through the thickness and Reissner-Mindlin-like partial derivative equations). Moreover, it was numerically demonstrated that the Bending-Gradient solution asymptotically converges to the exact solution as the slenderness ratio goes to infinity. Thus, with mirror-symmetric laminates, the Bending-Gradient solution is the Saint-Venant solution for an out-of-plane loaded plate.

When the laminate is not mirror-symmetric, the Bending-Gradient gives less accurate results: the transverse shear distribution or the related in-plane displacement might not exactly converge to the exact solution. Several explanations are currently under investigation. Especially, in Part I we indicated that it was our choice to neglect the contribution to the stress energy of the membrane stress gradient, $\boldsymbol{N} \otimes \boldsymbol{\nabla}$. Neglecting this contribution explains the discrepancy observed when the membrane stress in not zero, which occurs when the plate is not mirror-symmetric.

Finally, in Part I we pointed out that the relevance of introducing the full bending gradient might be questionable since the Bending-Gradient is sometimes turned into a Reissner-Mindlin model. In the present paper, we provide answers. On the one hand, when dealing with highly anisotropic laminates, it is clear that all localization fields are relevant (see Section 4.3.2) and the distance with Reissner-Mindlin presented in Section 4.3.3 fully justifies the use of the Bending-Gradient. Furthermore, in upcoming work, the Bending-Gradient theory will be applied to periodic plates. It appears that the distance between Reissner-Mindlin and Bending-Gradient models is almost up to 80% with very common patterns. On the other hand, when studying the influence of isotropy on the shear constitutive equation in Section 3.3 we indicated that only Poisson's effect has an influence on warping. Since most conventional materials have almost identical Poissons's ratios, it is more relevant to use a Reissner-Mindlin model in these cases. Eventually, the distance between Reissner-Mindlin and Bending-Gradient models is an efficient tool for deciding which model is the most relevant.

6. Conclusion

In the present paper, we provided first applications using the Bending-Gradient plate theory. We introduced Voigt notation which enables easier analytical computations and prepares finite elements implementation. Then the influence of material symmetries was associated to in-plane strain gradient elasticity. Closed-form solutions for cylindrical bending were fully derived, applied to laminates and compared to Reissner-Mindlin and finite elements approximations. The main conclusion is that the Bending-Gradient gives good predictions of both deflection and shear stress distributions in many material configuration. It is also the Saint-Venant solution when membrane stresses are fully uncoupled from bending moments and generalized shear stresses. Finally, with usual laminated plates, we demonstrated that the Bending-Gradient cannot be reduced to a Reissner-Mindlin plate model.

Several outlooks are under consideration. First, this plate theory can be extended to periodic plates such as sandwich panels (Lebée and Sab, 2010c,d). Second, the estimation of the influence of the membrane stress gradient on the quality of the shear stress estimation should be studied in detail. Finally, since we have a Saint-Venant solution, it is worth analyzing the shift with more refined approximations such as layerwise models or even full 3D finite elements when it is necessary to locally refine the analysis as illustrated in Amini et al. (2009) among others.

References

ABAQUS, 2007. ABAQUS/Standard user's manual, version 6.7.

Amini, A. M., Dureisseix, D., Cartraud, P., 2009. Multi-scale domain decomposition method for large-scale structural analysis with a zooming technique: Application to plate assembly. International Journal for Numerical Methods in Engineering 79 (4), 417–443.
URL http://dx.doi.org/10.1002/nme.2565

Auffray, N., Bouchet, R., Bréchet, Y., 2009. Derivation of anisotropic matrix for bi-dimensional strain-gradient elasticity behavior. International Journal of Solids and Structures 46 (2), 440 – 454.
URL http://www.sciencedirect.com/science/article/B6VJS-4TGHNGT-1/2/9d1bdfdd8fd533559bdf661d88c1186d

Caillerie, D., 1984. Thin elastic and periodic plates. Mathematical Methods in the Applied Sciences 6 (2), 159 – 191.

Caron, J. F., Diaz, A. D., Carreira, R. P., Chabot, A., Ehrlacher, A., May 2006. Multi-particle modelling for the prediction of delamination in multi-layered materials. Composites Science And Technology 66 (6), 755–765.

Carrera, E., 2002. Theories and finite elements for multilayered, anisotropic, composite plates and shells. Archives Of Computational Methods In Engineering 9 (2), 87–140.

Carrera, E., Sep. 2003. Theories and finite elements for multilayered plates and shells: A unified compact formulation with numerical assessment and benchmarking. Archives of Computational Methods in Engineering 10 (3), 215–296.
URL http://dx.doi.org/10.1007/BF02736224

Dallot, J., Sab, K., 2008. Limit analysis of multi-layered plates. part ii: Shear effects. Journal Of The Mechanics And Physics Of Solids 56 (2), 581–612.

Diaz Diaz, A., Caron, J.-F., Carreira, R. P., Dec. 2001. Model for laminates. Comptes Rendus de l'Académie des Sciences - Series IIB - Mechanics 329 (12), 873–879.
URL http://www.sciencedirect.com/science/article/B6W82-44RNNDJ-6/2/e596e50c0f033131f22c125aa605c234

Diaz Diaz, A., Caron, J. F., Ehrlacher, A., May 2007. Analytical determination of the modes i, ii and iii energy release rates in a delaminated laminate and validation of a delamination criterion. Composite Structures 78 (3), 424–432.

Hadj-Ahmed, R., Foret, G., Ehrlacher, A., Aug. 2001. Stress analysis in adhesive joints with a multiparticle model of multilayered materials (m4). International Journal Of Adhesion And Adhesives 21 (4), 297–307.

Lebée, A., Sab, K., 2010a. A bending gradient model for thick plates, part I: Theory. submitted.

Lebée, A., Sab, K., Apr. 2010b. A cosserat multiparticle model for periodically layered materials. Mechanics Research Communications 37 (3), 293–297.
URL http://www.sciencedirect.com/science/article/B6V48-4Y95TX1-1/2/6e88981818134d425cae268adda40a97

Lebée, A., Sab, K., 2010c. Reissner-mindlin shear moduli of a sandwich panel with periodic core material. In: Mechanics of Generalized Continua. Vol. 21 of Advances in Mechanics and Mathematics. Springer New York, pp. 169–177.
URL http://dx.doi.org/10.1007/978-1-4419-5695-8_18

Lebée, A., Sab, K., Sep. 2010d. Transverse shear stiffness of a chevron folded core used in sandwich construction. International Journal of Solids and Structures 47 (18-19), 2620–2629.
URL http://www.sciencedirect.com/science/article/B6VJS-506RCW3-1/2/70a945e9ed2d9b63a1eb91826f306304

Lewinski, T., 1991a. Effective models of composite periodic plates .1. asymptotic solution. International Journal Of Solids And Structures 27 (9), 1155–1172.

Lewinski, T., 1991b. Effective models of composite periodic plates .2. simplifications due to symmetries. International Journal Of Solids And Structures 27 (9), 1173–1184.

Lewinski, T., 1991c. Effective models of composite periodic plates .3. 2-dimensional approaches. International Journal Of Solids And Structures 27 (9), 1185–1203.

Naciri, T., Ehrlacher, A., Chabot, A., Mar. 1998. Interlaminar stress analysis with a new multiparticle modelization of multilayered materials (M4). Composites Science and Technology 58 (3-4), 337–343.
URL http://www.sciencedirect.com/science/article/B6TWT-3VCT890-3/2/8c268c8be97bf620d79000db44514ed2

Nguyen, T.-K., Sab, K., Bonnet, G., Mar. 2008a. First-order shear deformation plate models for functionally graded materials. Composite Structures 83 (1), 25–36.
URL http://www.sciencedirect.com/science/article/B6TWP-4N9DK2S-1/2/eb8bc31778e4482441c248081538b997

Nguyen, T.-K., Sab, K., Bonnet, G., Dec. 2008b. Green's operator for a periodic medium with traction-free boundary conditions and computation of the effective properties of thin plates. International Journal of Solids and Structures 45 (25-26), 6518–6534.
URL http://www.sciencedirect.com/science/article/B6VJS-4T8HHHD-3/2/16596be818a460bd68de55625a89a3c7

Nguyen, V.-T., Caron, J.-F., Sab, K., 2005. A model for thick laminates and sandwich plates. Composites Science and Technology 65 (3-4), 475 – 489.
URL http://www.sciencedirect.com/science/article/B6TWT-4DXC35K-1/2/a05ad2e465b63e1a5af709a0d56ff9ec

Noor, A. K., Malik, M., Feb. 2000. An assessment of five modeling approaches for thermo-mechanical stress analysis of laminated composite panels. Computational Mechanics 25 (1), 43–58.

Pagano, N., 1969. Exact solutions for composite laminates in cylindrical bending. Journal of Composite Materials 3 (3), 398–411.
URL http://jcm.sagepub.com/cgi/content/abstract/3/3/398

Pagano, N., 1970a. Exact solutions for rectangular bidirectional composites and sandwich plates. Journal of Composite Materials 4 (1), 20–34.
URL http://jcm.sagepub.com/cgi/content/abstract/4/1/20

Pagano, N., 1970b. Influence of shear coupling in cylindrical. bending of anisotropic laminates. Journal of Composite Materials 4 (3), 330–343.
URL http://jcm.sagepub.com/cgi/content/abstract/4/3/330

Reddy, J. N., Sep. 1989. On refined computational models of composite laminates. International Journal For Numerical Methods In Engineering 27 (2), 361–382.

Reissner, E., 1945. The effect of transverse shear deformation on the bending of elastic plates. Journal of Applied Mechanics 12, 68–77.

Vlasov, V. Z., 1961. Thin-walled elastic beams. National Science Foundation and Department of Commerce.

Whitney, J., 1972. Stress analysis of thick laminated composite and sandwich plates. Journal of Composite Materials 6 (4), 426–440.

Yu, W., Hodges, D. H., Volovoi, V. V., Oct. 2002. Asymptotic generalization of reissner-mindlin theory: accurate three-dimensional recovery for composite shells. Computer Methods in Applied Mechanics and Engineering 191 (44), 5087–5109. URL http://www.sciencedirect.com/science/article/B6V29-46V4RGP-6/2/2ffe45f2b95c3216f04307dcc4087900

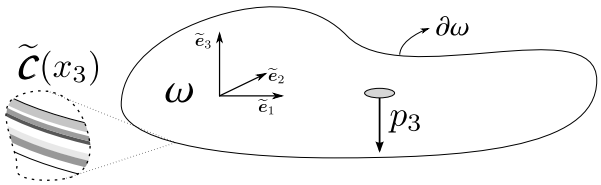

Figure 1: The plate configuration

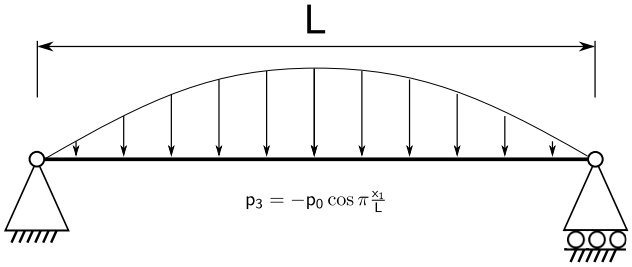

Figure 2: Pagano's cylindrical bending configuration ($n = 1$)

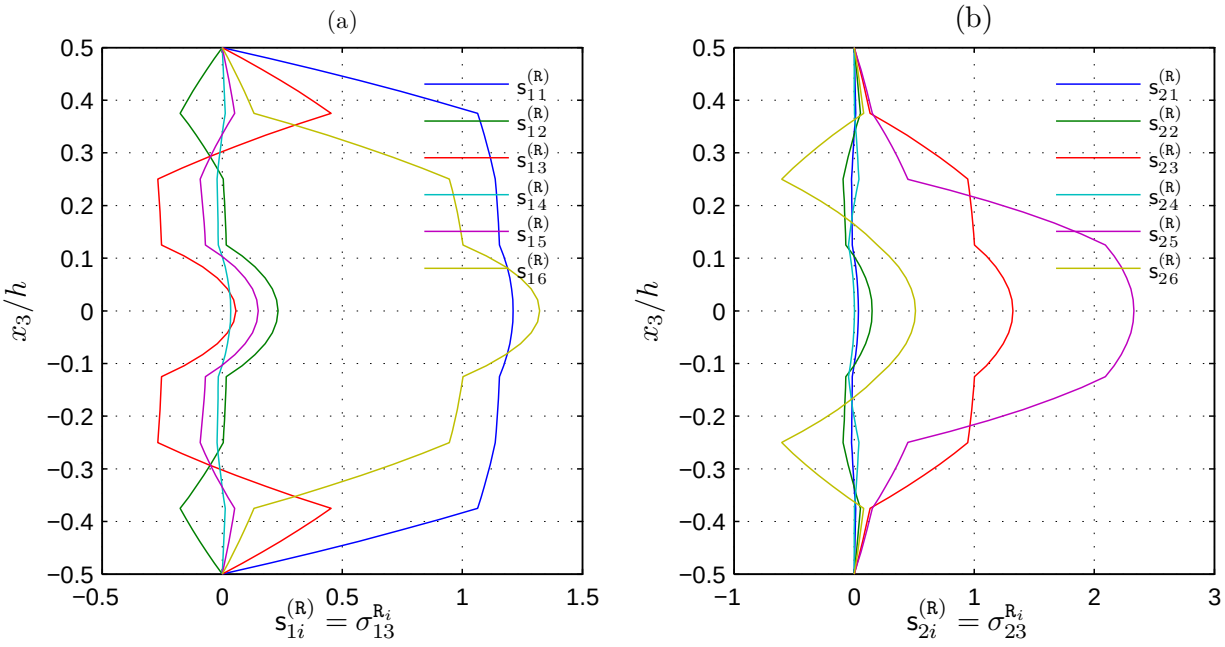

Figure 3: Bending gradient localization shear distributions through the thickness for a $[0°, -45°, 90°, 45°]_s$ laminate

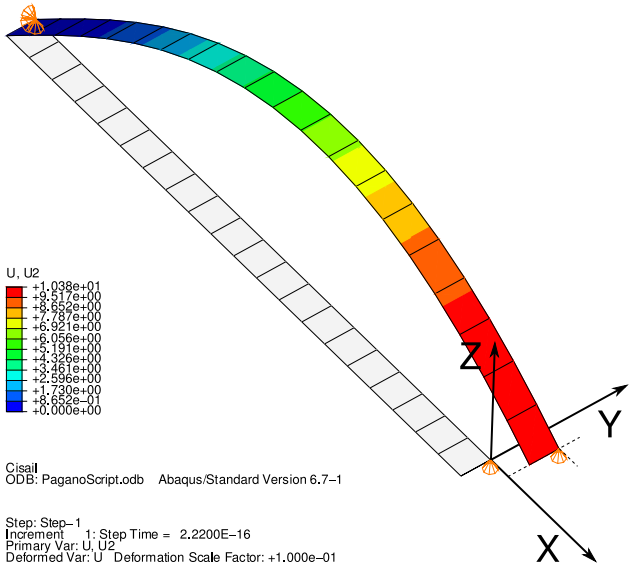

Figure 4: Finite Element undeformed and deformed mesh for an anisotropic laminate

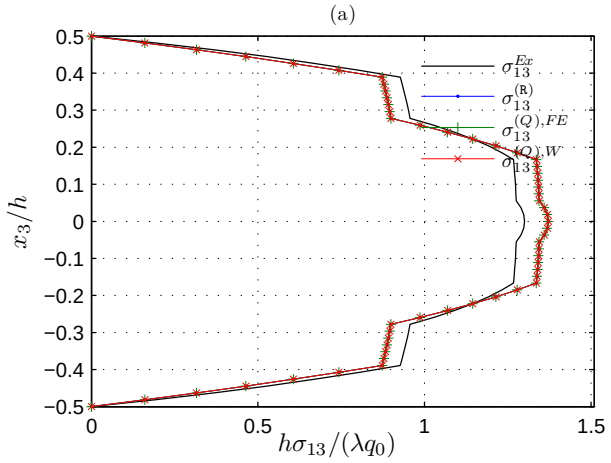

Figure 5: Normalized shear distribution σ_{13} at $x_1 = 0$ for a $[0°, 90°, 0°, 90°, 0°, 90°, 0°, 90°, 0°]$ laminate, $L/h = 4$, ($\sigma_{23} = 0$: symmetry). (*Ex*: exact, *BG*: Bending-Gradient, *RM*, *FE*: finite elements, *RM*, *W*:Whitney (1972)).

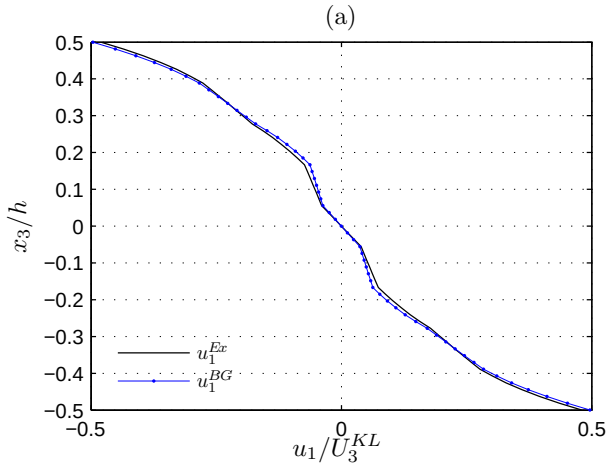

Figure 6: In-plane displacement distribution u_1 at $x_1 = 0$ for a $[0°, 90°, 0°, 90°, 0°, 90°, 0°, 90°, 0°]$ laminate, $L/h = 4$, ($u_2 = 0$: symmetry).

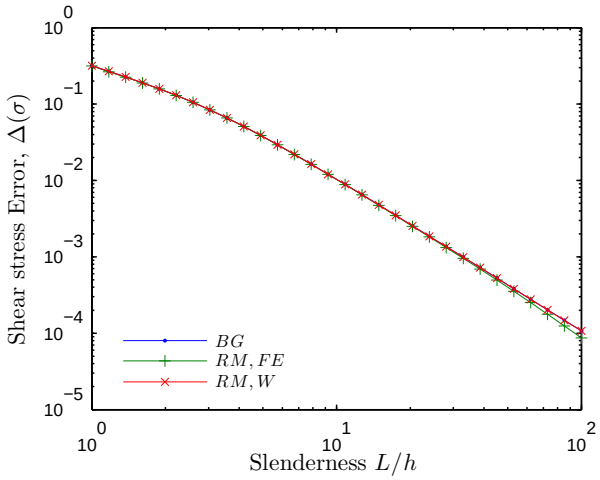

Figure 7: Shear stress distribution error versus slenderness ratio for a $[0°, 90°, 0°, 90°, 0°, 90°, 0°, 90°, 0°]$ laminate, (BG: Bending-Gradient, RM, FE: finite elements, RM, W:Whitney (1972))

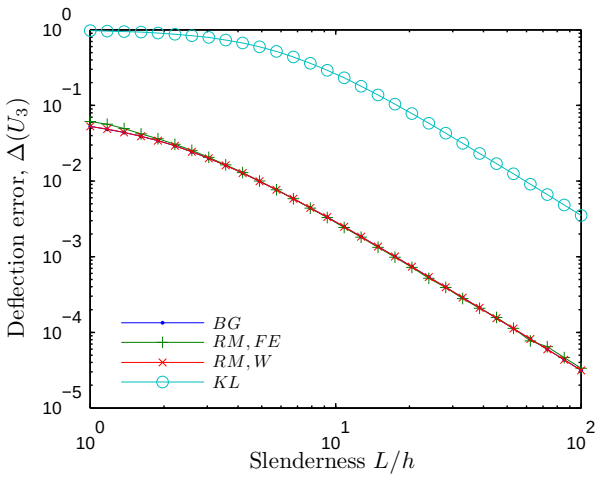

Figure 8: Deflection error versus slenderness ratio for a $[0°, 90°, 0°, 90°, 0°, 90°, 0°, 90°, 0°]$ laminate (BG: Bending-Gradient, RM, FE: finite elements, RM, W:Whitney (1972), KL: Kirchhoff-Love)

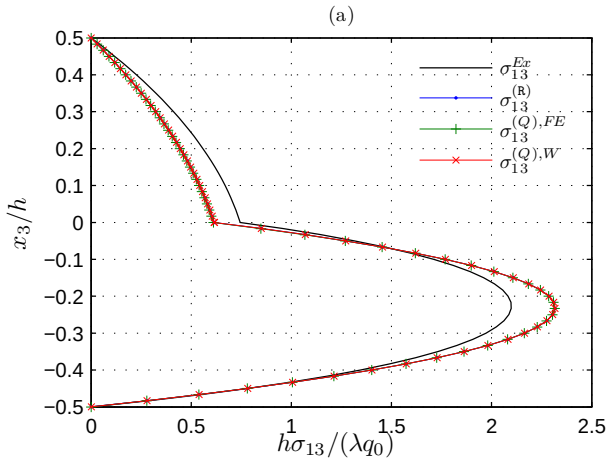

Figure 9: Normalized shear distribution σ_{13} at $x_1 = 0$ for a $[0°, 90°]$ laminate, $L/h = 4$, ($\sigma_{23} = 0$: symmetry).

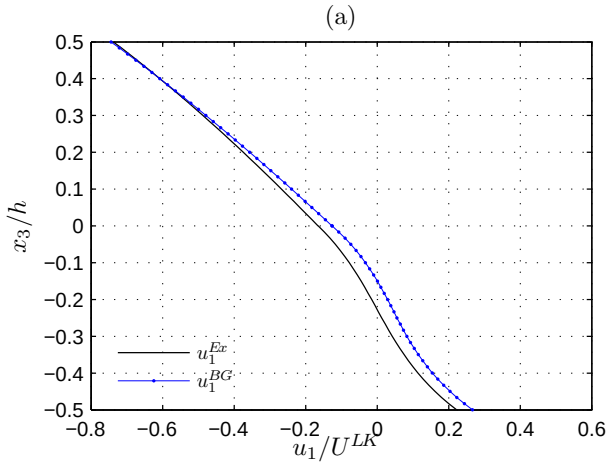

Figure 10: In-plane displacement distribution u_1 at $x_1 = 0$ for a $[0°, 90°]$ laminate, $L/h = 4$, ($u_2 = 0$: symmetry).

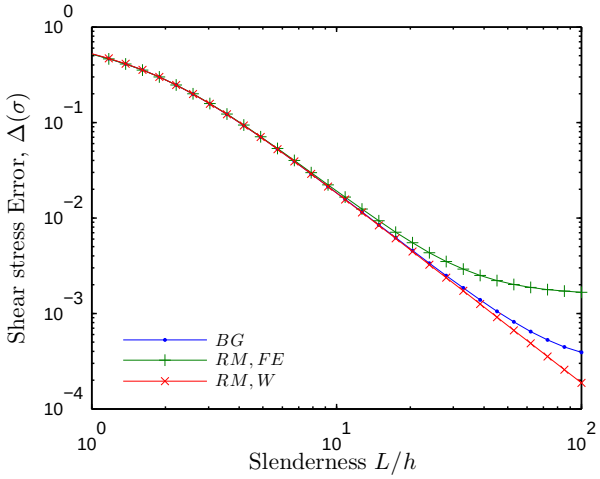

Figure 11: Shear stress distribution error versus slenderness ratio for a $[0°, 90°]$ laminate.

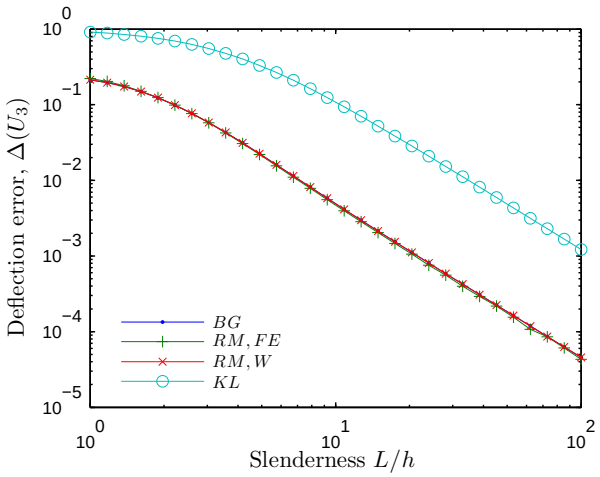

Figure 12: Deflection error versus slenderness ratio for a $[0°, 90°]$ laminate.

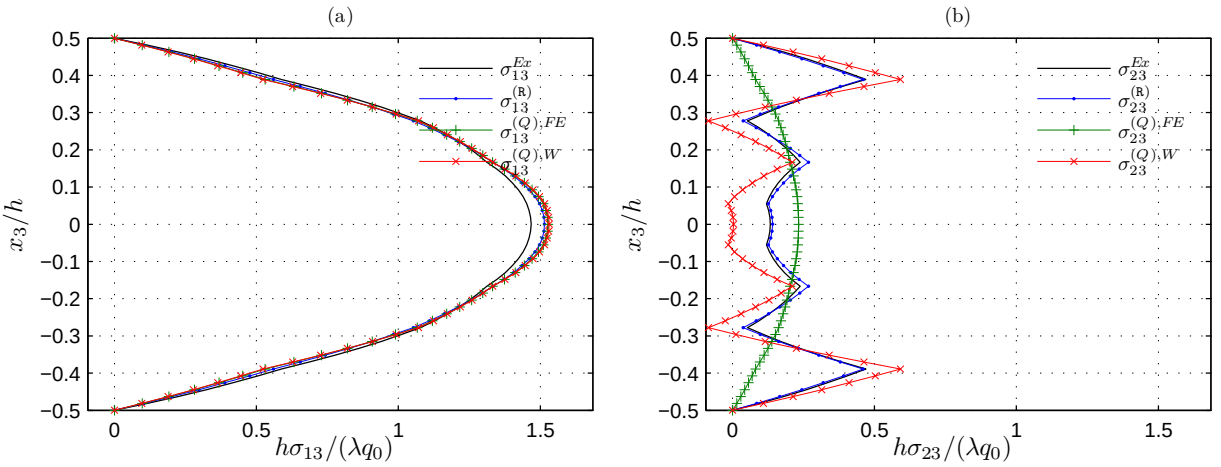

Figure 13: Normalized shear distribution in both directions at $x_1 = 0$ for a $[45°, -45°, 45°, -45°, 45°, -45°, 45°, -45°, 45°]$ laminate, $L/h = 4$, a) σ_{13} b) σ_{23}.

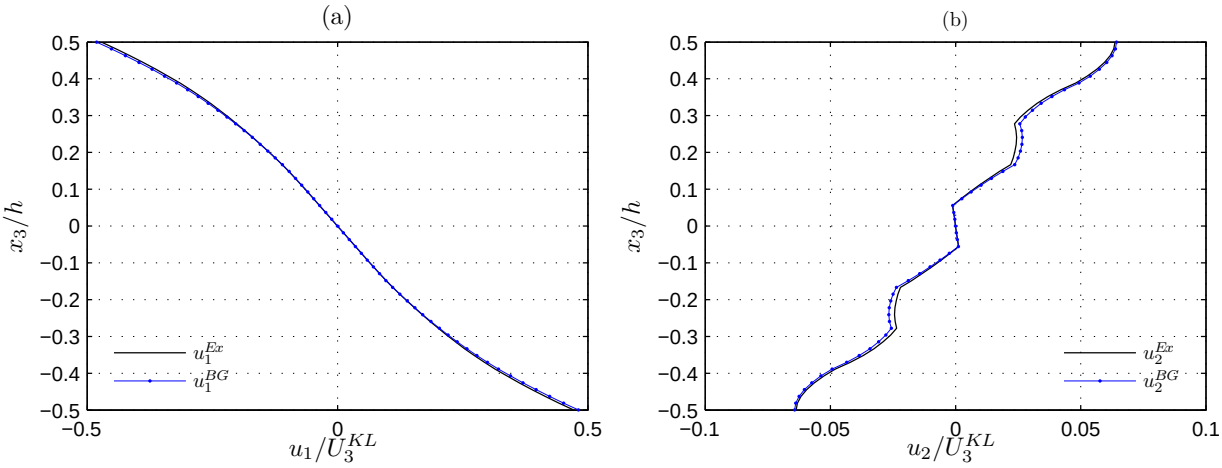

Figure 14: In-plane displacement distribution at $x_1 = 0$ for a $[45°, -45°, 45°, -45°, 45°, -45°, 45°, -45°, 45°]$ laminate, $L/h = 4$, a) u_1 b) u_2.

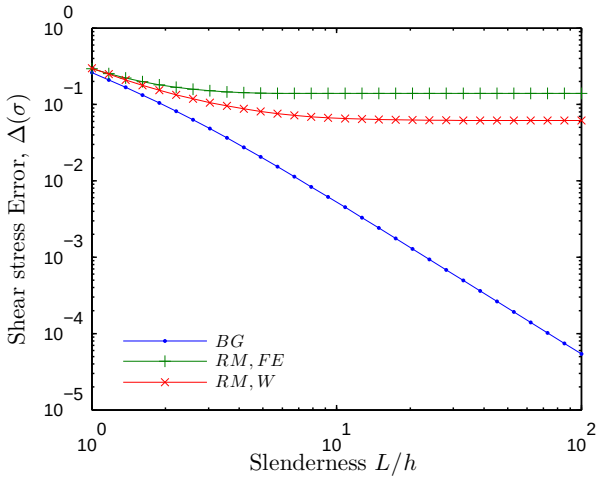

Figure 15: Shear stress distribution error versus slenderness ratio for a $[45°, -45°, 45°, -45°, 45°, -45°, 45°, -45°, 45°]$ laminate

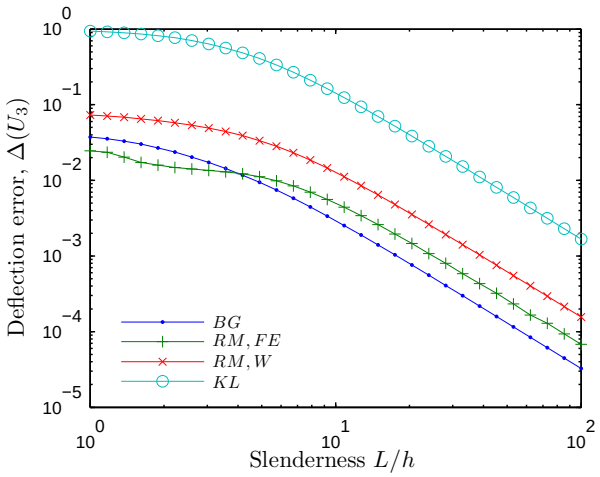

Figure 16: Deflection error versus slenderness ratio for a $[45°, -45°, 45°, -45°, 45°, -45°, 45°, -45°, 45°]$ laminate

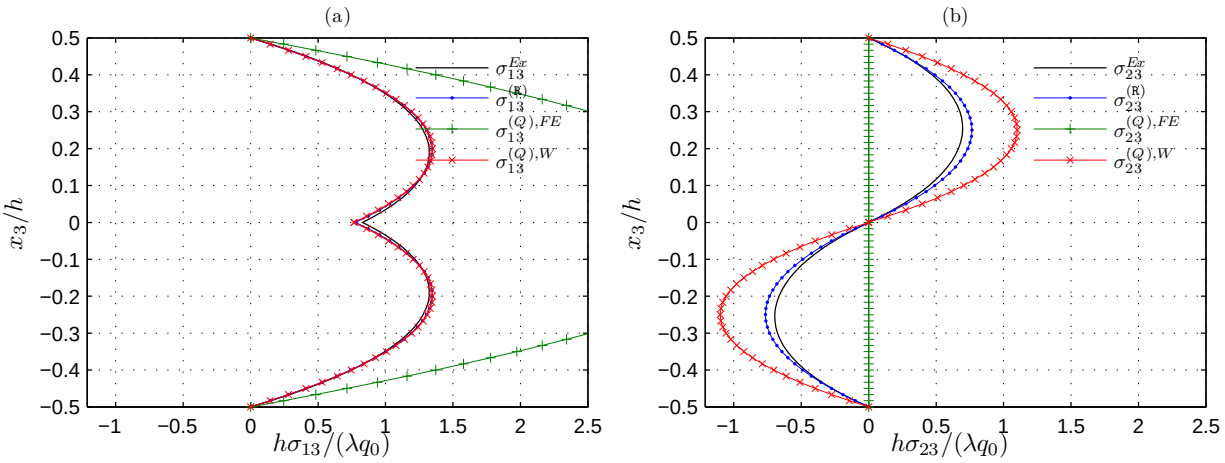

Figure 17: Normalized shear distribution in both directions at $x_1 = 0$ for a $[45°, -45°]$ laminate, $L/h = 4$, a) σ_{13} b) σ_{23}.

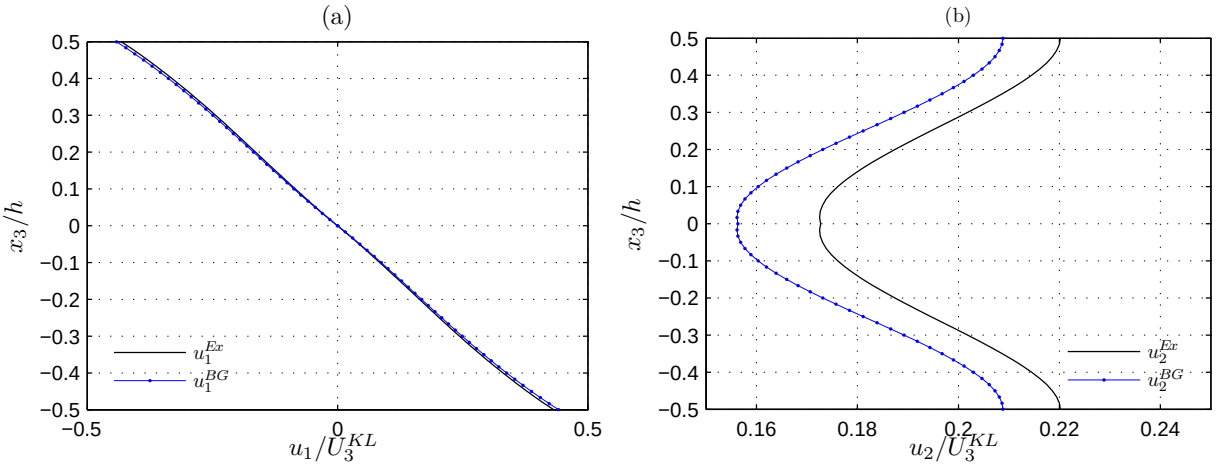

Figure 18: In-plane displacement distribution at $x_1 = 0$ for a $[45°, -45°]$ laminate, $L/h = 4$,, a) u_1 b) u_2.

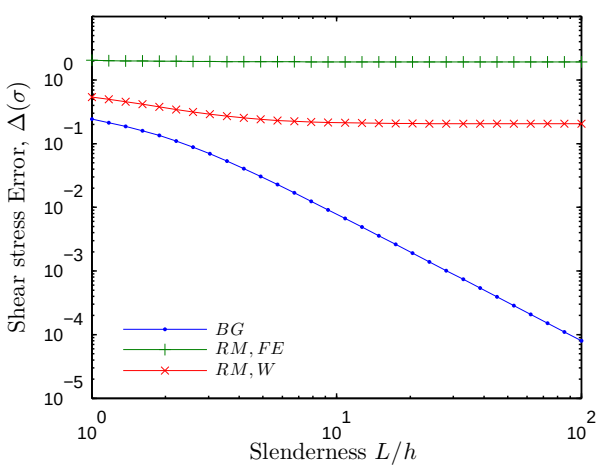

Figure 19: Shear stress distribution error versus slenderness ratio for a $[45°, -45°]$ laminate

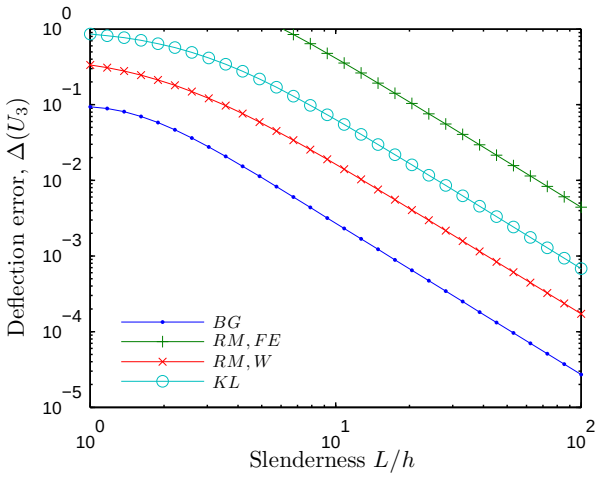

Figure 20: Deflection error versus slenderness ratio for a $[45°, -45°]$ laminate

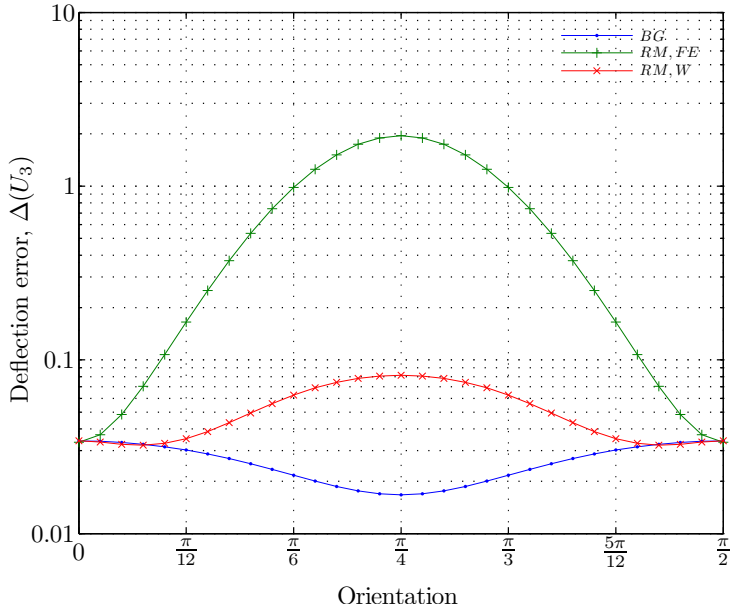

Figure 21: Deflection error versus bending direction for a $[0, 90°]$ laminate, $L/h = 4$